Arch. Mech., 50, 1, pp. 127–138, Warszawa 1998
FIFTY YEARS OF THE ARCHIVES OF MECHANICS

Effect of miss-distance on the airfoil-vortex interaction Numerical study

J. PIECHNA and A.P. SZUMOWSKI (WARSZAWA)

THE EFFECT of a strong vortex interacting with an airfoil flow is investigated numerically. The finite volume method for Euler equations is applied. Instantanous flow patterns, including pressure distributions along the airfoil and lift coefficients, were calculated for various miss-distances of the vortex passing parallel to the airfoil plane. It was found that the effects of interaction are much stronger when the vortex approaching the airfoil accelerates the flow at the pressure surface than in the case when the vortex decelerates the flow at the suction surface.

1. Introduction

IN CERTAIN CASES of helicopter flight, e.g. descent with deep turns or low-powered approach to landing, the rotor blade tip vortices strongly disturb the flow at the following blades. As a result, the blade loading considerably varies. This leads to vibrations of the blade and of the remaining elements of the helicopter structure. The variations of blade loading are accompanied by impulsive noise of high intensity.

The strongest effects of the airfoil-vortex interaction (AVI) occur when the vortex passes parallel and close to the airfoil plane. This was the main reason why the majority of the investigators who studied the AVI phenomenon considered two-dimensional model of interaction.

The vortex filament can pass at various miss-distances along both the upper and bottom surfaces of the airfoil. When it is equal to zero, a head-on impact occurs. This problem was investigated by LEE and BERSHADER [1, 2]. They solved the Navier–Stokes equations using a fifth order upwind scheme based on Osher-type of flux differencing. The isolines of density calculated by the above authors qualitatively coincide with those observed in the corresponding interferometric photographs. The sound wave which appears due to an expansion of high pressure air in the stagnation region was also predicted in the papers mentioned above. Pressure in the stagnation region increases when the vortex approaches the leading edge.

Variations of the surface pressure during the AVI for the vortex passing under the airfoil plane (increasing the flow velocity along the bottom surface of the airfoil) were calculated by DAMODARAN and CAUGHEY [3], EHRENFRIED [4] and GALLMAN [5]. The unsteady Euler equations [3, 4] or full-potential equation for transonic flow [5] were solved. DAMODARAN and CAUGHEY [3] and EHRENFRIED [4] noted a strong influence of the vortex on the lift and pitching moment

coefficients. Unfortunately, only one value of the miss-distance, equal to a quarter of the chord lengh, was considered by the above authors.

In the present work, an effect of miss-distance for the vortex passing over or under the NACA 0012 airfoil at 0 deg. angle of attack is considered. The miss-distance was changed in the range from -0.5 to $+0.2$ chords. A constant flow Mach number at infinity $M_\infty = 0.69$ and a constant circulation of a clockwise rotating vortex were assumed.

2. Equations

A coherent vortex of relative core radius $r/c = 0.045$ (r_0 – core radius, c – chord length of the airfoil) which is the subject of the present calculations causes rapid changes of actual flow properties during its passage along the airfoil. It can be supposed that these changes are controlled, first of all, by inertia effects but not by viscous ones.

By this assumption the Euler equations seem to be adequate for these calculations.

The two-dimensional Euler equations in integral form are as follows:

$$\frac{\partial}{\partial t}\int_S U\,ds + \int_L F\,dy + \int_L G\,dx = 0, \tag{1}$$

where

$$U = \begin{pmatrix} \varrho \\ \varrho u \\ \varrho v \\ e \end{pmatrix}, \qquad \begin{pmatrix} \varrho u \\ \varrho u^2 + p \\ \varrho uv \\ (e+p)u \end{pmatrix}, \qquad G = \begin{pmatrix} \varrho v \\ \varrho uv \\ \varrho v^2 + p \\ (e+p)v \end{pmatrix},$$

$$e = \varrho\frac{(u^2+v^2)}{2} + p/(\gamma - 1).$$

The first integral is related to the control area S and the remaining ones to the control circuit L (encircling the control area).

3. Boundary and initial conditions

The calculations performed in the present work correspond to experimental investigations of the AVI process with the use of shock tubes. To reproduce the experimental conditions, a control area shown in Fig. 1 is considered. Its upper and bottom surfaces correspond to the shock tube walls. Hence, the fluxes accross these walls are assumed to be zero. The remaining surfaces represent the cross-sections of the shock tube located upstream and downstream of the test airfoil. For these surfaces, a one-dimensional Riemann flow is considered.

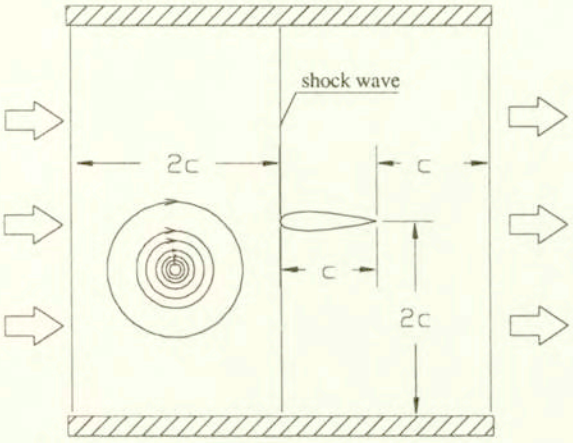

FIG. 1. Control area, $c = 120$ mm.

For the initial conditions it is assumed that the shock wave running in motionless air reaches the leading edge of the airfoil. The shock wave is followed by an axisymmetric vortex convected in a uniform flow. The vortex center in the initial phase of computation is located at half the distance between the shock front and the upstream control surface. It is assumed that the flow velocity induced by the vortex at the upper and bottom walls, as well as at the upstream cross-section and at the shock front, is small enough to be neglected. For the vortex considered (see below) it is under 5% of the flow velocity behind the shock wave. The calculations were stoped when the vortex leaves the trailing edge of the airfoil.

The flow velocity induced by the vortex for the initial phase of interaction is obtained from the following relationship:

$$V_\theta = \frac{\Gamma}{2\pi r} \frac{r^2(2+\alpha)}{r^2 \exp\left(\alpha(r-r_0)/r_0\right) + (1+\alpha)r_0^2}, \tag{2}$$

where V_θ – tangential velocity, r_0 – vortex core radius, Γ_0 – circulation at $r = r_0$, α – coefficient controlling velocity distribution.

The coefficient strongly influences the velocity distribution outside the vortex core but weakly inside it (Fig. 2).

For the experimental data which can be found in Ref. [6] $\alpha = 0.15$. For this α the velocity decay (in the radial direction) in the vortex is much stronger than for the clasical vortex model with $\alpha = 0$ (see Fig. 2). Taking into account this feature, one can consider a smaller control volume for $\alpha > 0$ than in the case of the clasical vortex. The pressure distribution corresponding to $V_\theta(r)$ can be found using the momentum

$$\frac{p}{r} = \frac{\varrho V_\theta^2}{r} \tag{3}$$

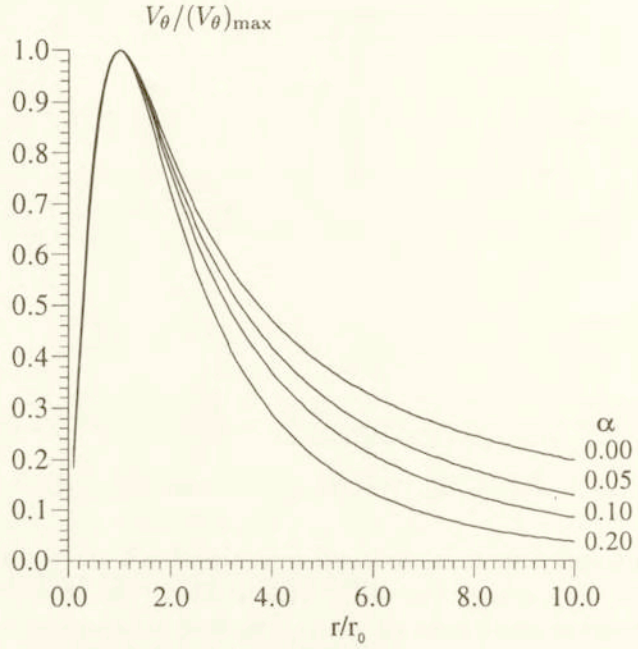

FIG. 2. Velocity distributions in the vortex.

and energy equation for adiabatic flow:

$$\frac{\gamma}{\gamma-1}\frac{p}{\varrho}+\frac{V_\theta^2}{2}=\frac{\gamma}{\gamma-1}\frac{p_\infty}{\varrho_\infty}, \tag{4}$$

where p_∞ and ϱ_∞ mean the pressure and density far from the vortex core, respectively.

The parameters Γ_0, r_0 and α in Eq. (1) can be chosen to match the real pressure distribution in the vortex. To obtain these parameters the pressure in the vortex center, the maximum of pressure derivative $(dp/dr)_{\max}$ and the radius corresponding to $(dp/dr)_{\max}$ determined from the measured function $p(r)$ can be used. The apropriate procedure is presented in Ref. [6]. In the present calculations the following values for Γ_0, r_0/c and α were assumed: 50 m^2/s, 0.045, 0.15, respectively. These values correspond to the measured pressure distribution in the vortex presented in Ref. [6].

4. Numerical procedure

The finite volume method is used. Equation (1) for a cell j of finite area ΔS yields:

$$\frac{dU_j}{dt}=\frac{1}{\Delta S}\sum(F\Delta y+G\Delta x). \tag{5}$$

In case of a quadrilateral cell (Fig. 3) the right-hand side of the above equation is

$$\frac{1}{\Delta S}\begin{Bmatrix} -(F_{i+1/2,j})(y_P - y_Q) + (G_{i+1/2,j})(x_P - x_Q) \\ -(F_{i-1/2,j})(y_R - y_S) + (G_{i-1/2,j})(x_R - x_S) \\ -(F_{i,j+1/2})(y_S - y_P) + (G_{i,j+1/2})(x_S - x_P) \\ -(F_{i,j-1/2})(y_Q - y_R) + (G_{i,j-1/2})(x_Q - x_R) \end{Bmatrix}.$$

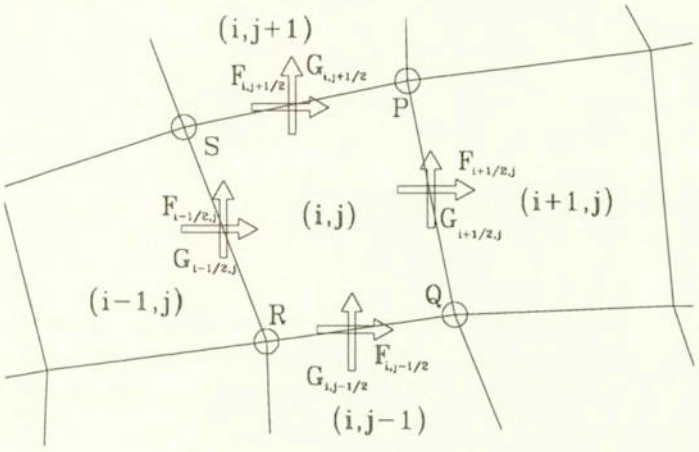

FIG. 3. Notation of the fluxes.

Each flux vector shown in Fig. 3 is composed of two terms, e.g.

$$F_{i+1/2,j} = F^{+}_{i,j} + F^{-}_{i+1,j}\,. \tag{6}$$

The first and the second term on the right-hand side are the forward and the backward contributions of the fluxes produced by the neighbouring cells i, j and $i+1, j$, respectively (Fig. 4).

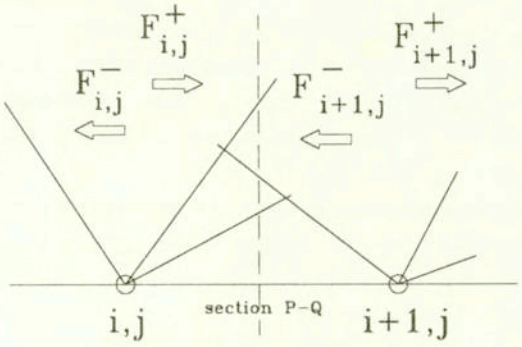

FIG. 4. Flux splitting.

The contributions are obtained by splitting the flux vector F, in the way proposed by VAN LEER [7], as follows:

for $-a < u < a$ (a means the speed of sound)

$$F^{\pm} = \left\{ \begin{array}{l} f^{\pm} \\ f^{\pm}\left[(\gamma-1)u \pm 2a\right]/\gamma \\ f^{\pm}v \\ f^{\pm}\left\{\left[(\gamma-1)u \pm 2a\right] / \left[2(\gamma^2-1)\right] + v^2/2\right\} \end{array} \right\},$$

where

$$f^{\pm} = \varrho(u+a)^2/(4a)$$

for $u > a$

$$F^{+} = F, \qquad F^{-} = 0,$$

and for $u < -a$

$$F^{+} = 0, \qquad F^{-} = F.$$

The second order Runge–Kutta procedure was applied to integrate Eq. (5).

Almost 360 000 cells uniformly distributed in the control volume were used. Such a large number of cells was chosen to prevent numerical dispersion of the vortex during its passage.

5. Results

Figures 5 show the pressure isolines for six phases of the AVI process. The vortex was initially positioned under (at $h/c = -0.2$) or over ($h/c = 0.2$) the airfoil symmetry plane for the figures in the first and the second column, respectively. In Figs. 5 a and 5 g one can see the clockwise rotating vortex approaching the airfoil.

The vortex disturbs the bow shock wave which appears when the incident shock wave reflects at the leading section of the airfoil. Due to the vortex, the stagnation point leaves its initial position at the leading edge and shifts on to the upper surface independently of the vortex initial location ($h/c = -0.2$ and 0.2). However, beginning from the following phase when the vortex reaches the region very close to the leading edge, the flow patterns become strongly dependent on the vortex trajectory, i.e. on wheather the vortex passes over or under the airfoil. In the former case (Fig. 5 h) the stagnation point moves in the bottom surface of the airfoil. It comes back again to the leading edge after some delay (Fig. 5 j) as the vortex is being convected. The remaining flow region does not show remarkable changes.

In contrast to this, the latter case exhibits much stronger variations of the flow pattern. The vortex, when it passes the leading edge (Fig. 5 c), induces a supersonic flow region at the bottom surface of the airfoil. In this region there

is a shock wave. Simultaneously, a strong disturbance (compressive wave) is created at the leading section of the airfoil. It appears due to the expansion of the air in the stagnation region as the vortex passes the leading edge (the air in the stagnation region was initially compressed to high pressure owing to high velocity induced by the vortex). The compressibility wave which expands in the space under the airfoil is visible in Figs. 5 d – f. The shock wave in the supersonic flow region (Fig. 5 c) initially precedes the vortex and moves with it. However, the spacing between the shock wave and the vortex decreases. In the phase shown in Fig. 5 d the shock is in the plane normal to the airfoil and crossing the vortex core. In the following phases (Fig. 5 e, f) when the vortex passes the compression region at the trailing section of the airfoil, the shock wave disappears. The bow shocks visible in Fig. 5 e at both the upper and the bottom surfaces, form due to steepening of the compressibility waves. They appear at the trailing edge when it is left by the incident shock wave. Additional shocks emerge at the trailing edge when the vortex approaches it (Fig. 5 f).

The pressure distributions along the upper and bottom surfaces of the airfoil, corresponding to instantaneous flow patterns described above, are shown in Figs. 6 a – f. They are compared with those for the flow without vortex. For the phase of interaction shown in Fig. 6 a, at which the vortex only weakly influences the airfoil flow, the pressure distributions along the upper and bottom surfaces are very close to those obtained for case without the vortex. The compressibility waves mentioned above, induced by the incident shock wave when it leaves the trailing edge, can be observed in the trailing section. The difference between the pressure distributions increases as the vortex approaches the leading edge (Fig. 6 b). In the phase shown in Fig. 6 c, the supersonic flow region divided into two parts by a shock wave can be noted at the bottom surface. This suggests that the shock in this phase moves upstream and is followed by a compressive wave. The shock gains in strength during its motion down the airfoil. It achieves its maximum strength for the phase when it passes through the vortex (Fig. 5 d and 6 d). One can see that for the initial phases of the AVI, when the vortex passes the leading section, the average pressure at the bottom surface ($\overline{p}_b$) is lower than that at the upper surface ($\overline{p}_u$). The relationship between $\overline{p}_b$ and $\overline{p}_u$ changes as the vortex passes the airfoil, $\overline{p}_u$ increases whereas $\overline{p}_b$ decreases.

Eventually, for the vortex at the trailing edge, we have $\overline{p}_u < \overline{p}_b$. Variations of pressure do not disappear when the vortex leaves the airfoil. The experiments conducted in Ref. [8] prove that they exist for a relatively long time afterwards.

Analogous behaviour of the surface pressure can be also found for the vortex passing over the airfoil. In this case, however, the pressure variations are much weaker than for the vortex passing under the airfoil at the same miss-distance.

Histories of the lift coefficient (C_l) for four values of the miss-distance of the vortex passing under the airfoil are presented in Fig. 7. It can be noted that variations of C_l show cosine-like character. Its amplitude decreases with increasing miss-distance. Figure 8 shows a comparison of C_l for two vortex trajectories

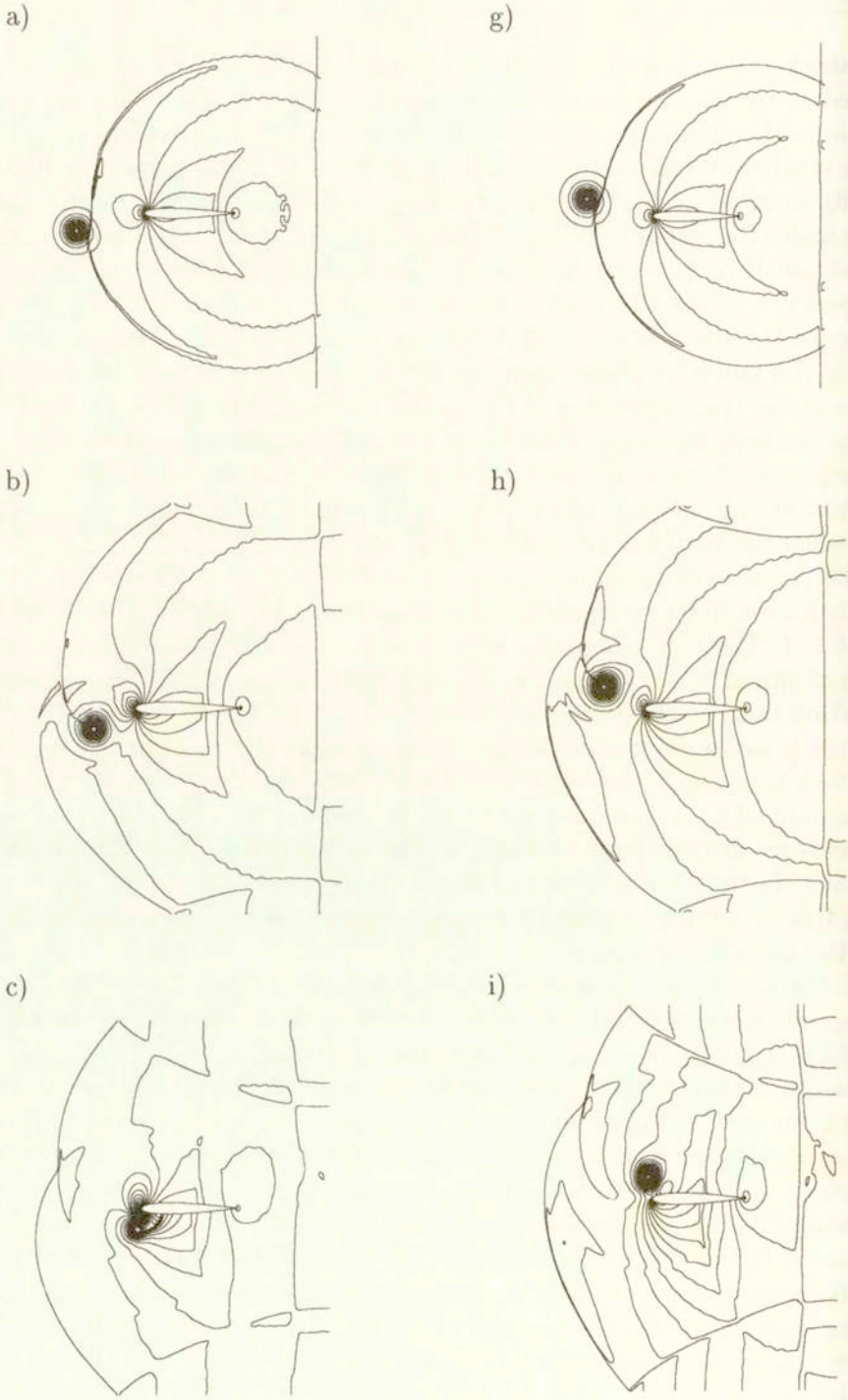

[FIG. 5]

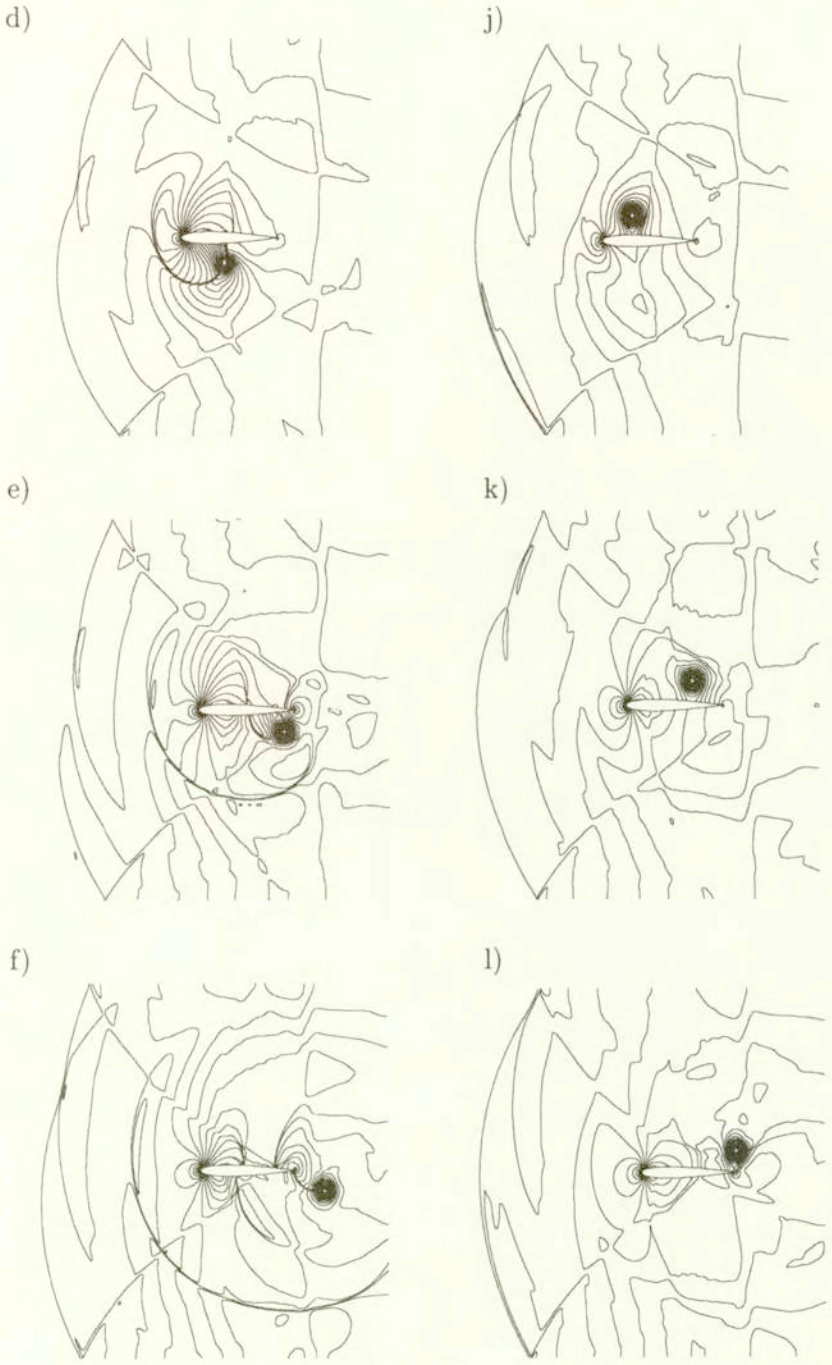

FIG. 5. Instantanous pressure isolines for the vortex passing under (first column) and over (second column) the airfoil. Delay in relation to the moment when the incident shock wave reaches the leading edge: (a,g) 0.508 ms, (b,h) 0.678 ms, (c,i) 0.848 ms, (d,j) 1.017 ms, (e,k) 1.186 ms, (f,l) 1.355 ms.

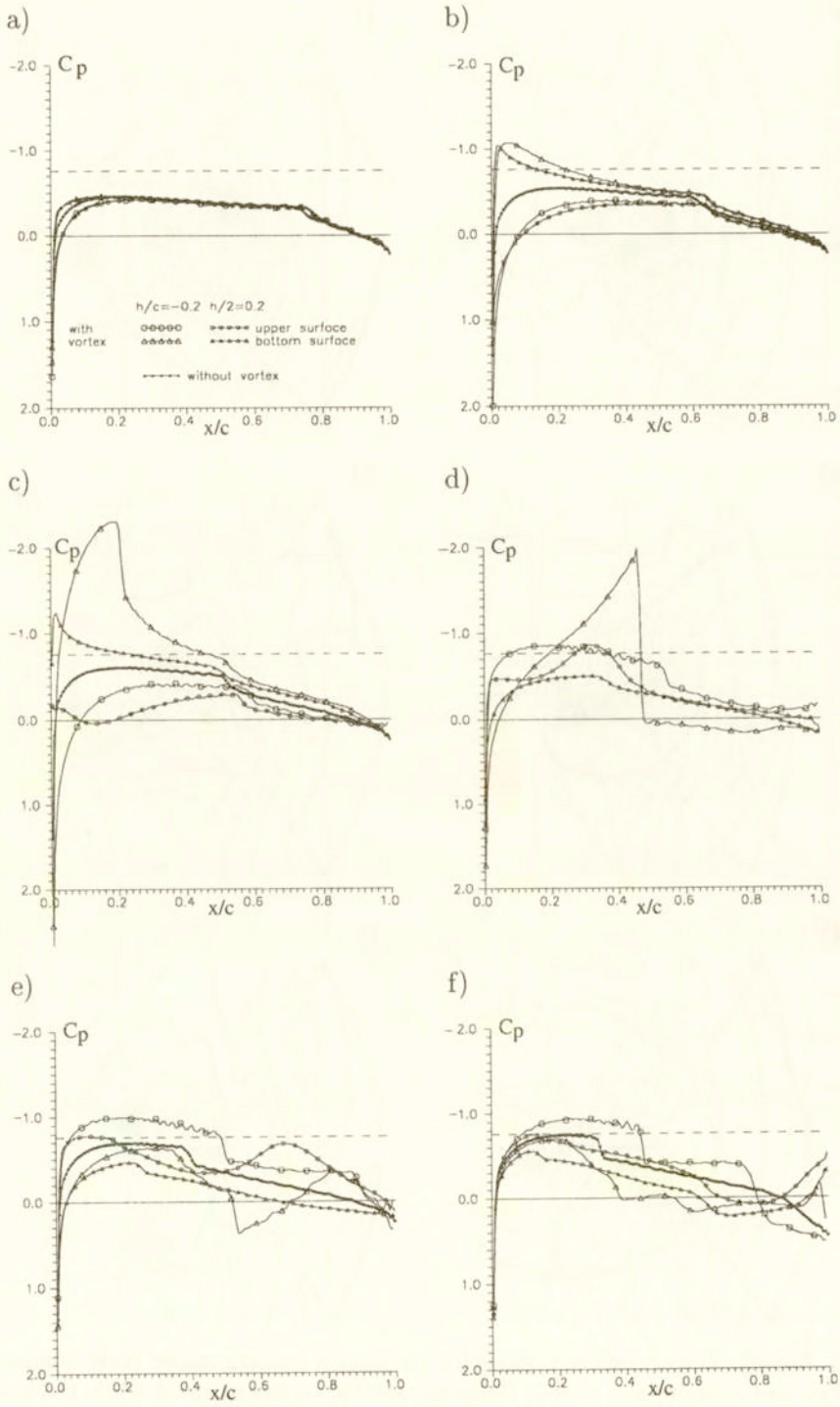

FIG. 6. Instantanous surface pressure coefficient (C_p) distributions corresponding to flow patterns shown in Fig. 5. Dashed line means sonic flow.

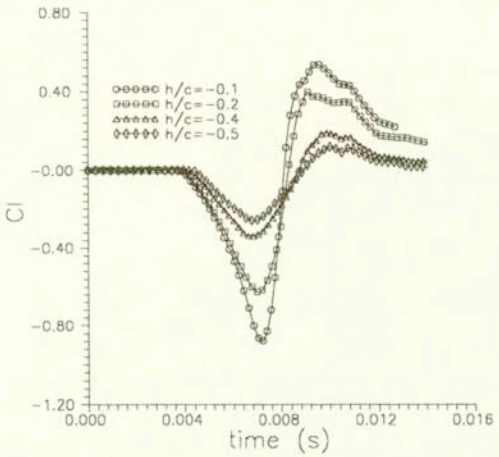

FIG. 7. Lift coefficients for various trajectories of the vortex passing under the airfoil.

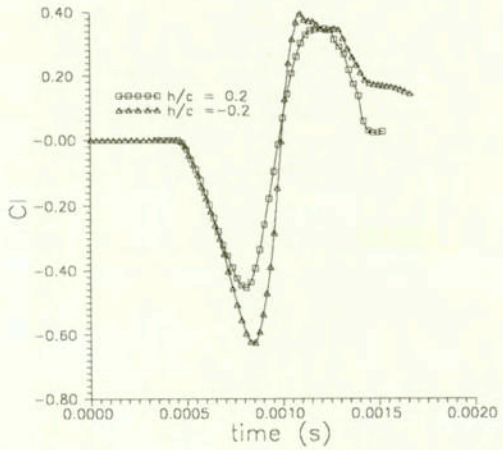

FIG. 8. Lift coefficients for the vortex passing over ($h/c = 0.2$) and under ($h/c = -0.2$) the airfoil.

$h/c = 0.2$ and $h/c = -0.2$. It is visible that the amplitude of C_l is larger for negative miss-distance.

6. Conclusions

Vortex trajectory appears to be an important parameter controlling the airfoil-vortex interaction. The effects of the AVI are much stronger when the vortex approaching to the airfoil accelerates the flow at the pressure surface of the airfoil than in the case when the vortex decelerates the flow at the suction surface. These cases correspond to the clockwise rotating vortex passing under or over the airfoil

considered in the present studies, respectively. The miss-distance strongly affects the instantaneous pressure distributions along the airfoil which leads to strong variations of the lift coefficient.

The background flow on which the vortex is superimposed has been induced in the present numerical investigation by a preceding shock wave passing along the airfoil at 0 deg. angle of attack. Nevertheless, the results obtained, at least qualitative, can be also considered for the case of fully developed steady background flow.

References

1. S. LEE and D. BERSHADER, *An experimental and computational study of 2-D parallel blade. Vortex interaction*, AIAA Paper, 91-3277.
2. S. LEE and D. BERSHADER, *Head-on parallel blade-vortex interaction*, AIAA J., **1**, 1, pp. 16–22, 1994.
3. S. DAMODARAN and D. CAUGHEY, *Finite-volume computation of inviscid transonic airfoil. Vortex interaction*, AIAA J., **26**, 11, pp. 1346–1352, 1988.
4. K. EHRENFRIED, *Numerische Untersuchung von Wirbel-Tragflügel-Wechselwirkungen im transsonischen Geschwindigkeitsbereich*, Max-Planck-Institut für Stroemungsforschung Report, 8, 1991.
5. J. GALLMAN, *Parametric computational study of isolated blade-vortex interaction noise*, AIAA J., **32**, 2, pp. 232–238, 1994.
6. A. SZUMOWSKI, J. PIECHNA, W. SELEROWICZ and G. SOBIERAJ, *Modified formula for the velocity distribution in a vortex*, J. Fluid Engng. [to be published].
7. B. VAN LEER, *Flux-vector splitting for the Euler equations*, Lecture Notes in Physics., **170**, pp. 507–512, 1982.
8. W. KAMIŃSKI and A. SZUMOWSKI, *Acoustic effects of parallel vortex-airfoil interaction*, J. Sound and Vibration, **183**, 2, 209–220, 1995.

WARSAW UNIVERSITY OF TECHNOLOGY
ul. Nowowiejska 24, 00-665 Warsaw.

Received June 20, 1997; new version October 30, 1997.